










Tailoring bistability in optical tweezers with vortex beams and spherical aberration

Arthur L. da Fonseca ^{1,2} Kainã Diniz ^{1,2} Paula B. Monteiro,³ Luís B. Pires ⁴ Guilherme T. Moura ^{1,2}
Mateus Borges ^{1,2} Rafael S. Dutra ⁵ Diney S. Ether, Jr. ^{1,2} Nathan B. Viana ^{1,2} and Paulo A. Maia Neto ^{1,2,*}

¹*Instituto de Física, Universidade Federal do Rio de Janeiro Caixa Postal 68528, Rio de Janeiro, Rio de Janeiro 21941-972, Brazil*

²*CENABIO—Centro Nacional de Biologia Estrutural e Bioimagem, Universidade Federal do Rio de Janeiro, Rio de Janeiro, Rio de Janeiro 21941-902, Brazil*

³*Instituto Federal de Santa Catarina, Campus Florianópolis, Av. Mauro Ramos, 950, Florianópolis, Santa Catarina 88020-300, Brazil*

⁴*Université de Strasbourg, CNRS, Institut de Science et d'Ingénierie Supramoléculaires, UMR 7006, F-67000 Strasbourg, France*

⁵*LISComp-IFRJ, Instituto Federal de Educação, Ciência e Tecnologia, Rua Sebastião de Lacerda, Paracambi, Rio de Janeiro 26600-000, Brasil*



(Received 1 November 2023; accepted 29 April 2024; published 3 June 2024)

We demonstrate a bistable optical trap by tightly focusing a vortex laser beam. The optical potential has the form of a Mexican hat with an additional minimum at the center. The bistable trapping corresponds to a nonequilibrium steady state, where the microsphere continually hops, due to thermal activation, between an axial equilibrium state and an orbital state driven by the optical torque. We develop a theoretical model for the optical force field, based entirely on experimentally accessible parameters, combining a Debye-type nonparaxial description of the focused vortex beam with Mie scattering by the microsphere. The theoretical prediction that the microsphere and the annular laser focal spot should have comparable sizes is confirmed experimentally by taking different values for the topological charge of the vortex beam. Spherical aberration introduced by refraction at the interface between the glass slide and the sample is considered and allows us to finetune between axial, bistable, and orbital states as the sample is shifted with respect to the objective focal plane. We find overall agreement between theory and experiment for a rather broad range of topological charges. Our results open the way for applications in stochastic thermodynamics, as they establish a control parameter—the height of the objective focal plane with respect to the glass slide—that allows us to shape the optical force field in real time and in a controllable way.

DOI: [10.1103/PhysRevResearch.6.023226](https://doi.org/10.1103/PhysRevResearch.6.023226)

I. INTRODUCTION

Optical tweezers [1–3] with structured light beams [4] allow for a vast range of applications in optical micromanipulation [5–10]. Photons in vortex beams carry orbital angular momentum [11], which can be exchanged with the trapped particle as an optical torque [12,13]. As a result of spin-orbit coupling [14–16], strong focusing of a circularly polarized vortex beam produces an annular focal spot whose properties depend on the relative sign between the orbital and spin angular momenta [17–22]. In the standard optical tweezers setup, such an annular spot provides for two very different trapping conditions. Particles smaller than the ring of maximum energy density resolve the spatial energy variation and, as a consequence, move along a circular orbit around the optical axis [23,24]. On the other hand, larger particles are expected to be trapped on a stable on-axis position [25,26].

In this paper, we demonstrate, both theoretically and experimentally, that bistable trapping is achieved as the orbital and axial states coexist in the intermediate size range. The trapping potential has the form of a Mexican hat with an additional minimum at the center. The onset of bistability as well as the transition from axial to orbital trapping can be controlled by adjusting the focal height with respect to the glass slide at the bottom of our sample. Indeed, as the spherical aberration phase introduced by refraction at the glass-water interface [27,28] is proportional to the focal height, we can switch from axial to bistable and then to orbital trapping by displacing the sample with the help of a piezoelectric nanopositioning system. By increasing the focal height, we first drive the Brownian particle from the equilibrium state in a harmonic potential to the regime with two distinct mesostates [29] characterized by different conformational free energies [30]. Then by further increasing the focal height, we implement a paradigmatic nonequilibrium steady state (NESS) [31], in which a colloidal particle is driven along a circular orbit by the nonconservative optical force component associated with the laser beam angular momentum. Thus, our system allows one to explore different models of stochastic thermodynamics [31,32] with a single platform disposing of a tunable parameter—the focal height.

To explain our experimental results, we extend the Mie-Debye spherical aberration (MDSA) theory of optical

*pamn@ifufrj.br

Published by the American Physical Society under the terms of the [Creative Commons Attribution 4.0 International license](https://creativecommons.org/licenses/by/4.0/). Further distribution of this work must maintain attribution to the author(s) and the published article's title, journal citation, and DOI.

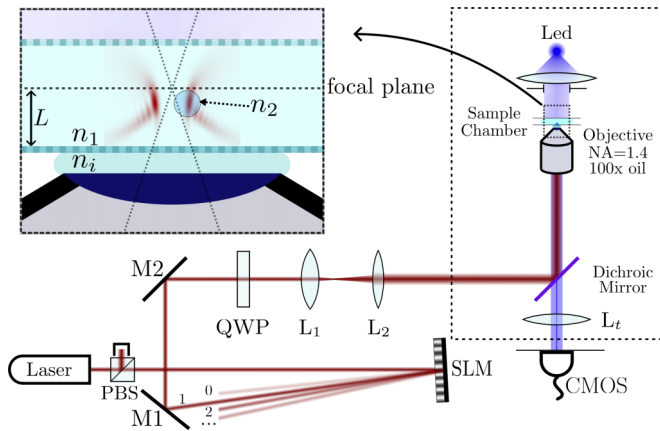


FIG. 1. Illustration of the experimental setup. The laser beam goes through a polarizing beam splitter (PBS) and is directed to the spatial light modulator (SLM). The first order of diffraction propagates through a quarter-wave plate (QWP) and, for values of ℓ up to 5, through a beam expander (lenses L1 and L2) toward the microscope (dotted frame). Inside the microscope, the beam is reflected by a dichroic mirror (DM) and then focused by an oil-immersion objective. The inset shows a magnified view of the sample region with the glass slide lying at its bottom. The refractive index mismatch between the glass slide (index n_i) and the aqueous medium filling the sample (index n_1) leads to the introduction of a spherical aberration phase upon refraction at the interface between the slide and the sample. Such a phase is proportional to the height L of the objective focal plane with respect to the slide, whose position is controlled by a piezoelectric nanopositioning stage (not shown). The resulting nonparaxial focused beam is indicated by the density plot of the electric energy density for $L = 10 \mu\text{m}$ (red). The inset also depicts a trapped microsphere of refractive index n_2 .

tweezers [33–36] by considering a vortex beam at the objective entrance port. The paraxial approximation is taken only at the entrance port, and the nonparaxial tightly focused trapping beam arises as a vector interference of spatial Fourier components [37]. Such a realistic description allows us to analyze in detail how the optical force field changes as the spherical aberration increasingly degrades the focal spot.

This paper is organized as follows. The experimental setup and the theoretical formalism are presented in Secs. II and III, respectively. Bistability is first discussed in the simpler scenario of ideal aberration-free trapping beams in Sec. IV A. Experimental results and a comparison with the theoretical description considering spherical aberration are presented in Secs. IV B and IV C, respectively. Section V is devoted to concluding remarks.

II. EXPERIMENTAL SETUP

The generation of structured light beams has been extensively discussed [38]. Here, we use a spatial light modulator (SLM) to synthesize a vortex beam with topological charge ℓ . Our setup is depicted in Fig. 1. We steer a horizontally polarized TEM_{00} laser beam (IPG photonics, model YLR-5-1064LP) with wavelength $\lambda_0 = 1064 \text{ nm}$ onto the SLM (Holoeye Photonics AG Pluto), in which we display an

overlap between the vortex phase and a linear ramp, producing several orders of diffraction.

As shown in Fig. 1, we propagate the first order of diffraction through a quarter-wave plate (QWP) to produce left-handed circular polarization and expand its beam waist w_0 so that the annular vortex beam slightly overfills the objective entrance port. The overfilling of the objective entrance port of radius $R_p = (2.80 \pm 0.05) \text{ mm}$ is such that the radius of maximum intensity

$$r_\ell = w_0 \sqrt{\frac{|\ell|}{2}} \quad (1)$$

is of the order of R_p . The reasons for selecting such a filling condition as well as the values of w_0 and r_ℓ are discussed in detail in Appendix A. We check the transverse profile of the vortex beam after expansion with the help of a scanning-slit beam profiler (ThorLabs BP209-VIS/M).

After reflection by a dichroic mirror, the vortex beam is strongly focused by the oil-immersion microscope objective [Nikon PLAN APO, 100 \times , numerical aperture (NA) = 1.4]. The sample chamber is contained by an O-ring on top of the glass slide and filled with a suspension of polystyrene microspheres (Polysciences, Warrington, PA) in water. The entire system is displaced vertically by a piezoelectric nanopositioning stage (Digital Piezo Controller E-710, Physik Instrumente), allowing us to change the distance L between the glass slide and the objective focal plane as depicted in the inset of Fig. 1. Since the spherical aberration phase introduced by refraction at the interface between the glass slide and the aqueous medium is proportional to L [27], we can tailor different trapping regimes by finetuning such a distance. To provide room for trapping with small and moderate values of L , we displace the diffraction focus upward with respect to the objective focal plane by allowing the vortex beam to develop a finite curvature as it propagates toward the back aperture of the objective. According to the displacement theorem [39], the resulting curvature of field leads to a global shift of the laser focal spot without changing the amount of spherical aberration.

The Köhler illumination by an LED source (wavelength 470 nm) is also depicted in Fig. 1. Light scattered by the microspheres is collected by the objective and goes through the dichroic mirror and the microscope tube lens L_t . The resulting images are recorded by a CMOS camera (Hamamatsu Orca-Flash 2.8 C11440-10C) with acquisition rates of 50 fps ($\ell = 4, 5$) and 30 fps ($\ell = 8, 11$). We use digital videomicroscopy to determine the microsphere position. We apply a threshold and then extract the position from the center of mass of the resulting grayscale image.

III. MDSA THEORY OF OPTICAL TRAPPING WITH VORTEX BEAMS

The Mie-Debye theory of optical optical tweezers [33,34] combines a nonparaxial Debye-type model of a strongly focusing beam [37] with Mie scattering by the trapped microsphere. An important extension to include the spherical aberration introduced by focusing through the interface between the glass slide and the sample was developed in Refs. [35,36] (MDSA theory). When astigmatism is also

included, good agreement with experimental data for the trap stiffness [40,41] and the vorticity at the focal point [42] is found, with no fitting. Here, we further extend MDSA theory to account for focusing of vortex beams, opening the way for a quantitative description of optical tweezers experiments with structured light beams and their several applications [5–10,12,13].

For simplicity, we neglect astigmatism and model the paraxial beam entering the objective back aperture as a circularly polarized Laguerre-Gaussian $LG_{0\ell}$ mode with radial order $p = 0$. In cylindrical coordinates, the corresponding electric field reads

$$\mathbf{E}_p(\rho, \phi, z) = E_0 \left(\frac{\sqrt{2}\rho}{w_0} \right)^{|\ell|} \exp\left(-\frac{\rho^2}{w_0^2}\right) \exp(i\ell\phi) \times \exp(ik_0 z) \hat{\mathbf{e}}_\sigma. \quad (2)$$

Here, $k_0 = 2\pi/\lambda_0$ is the laser wave number and $\hat{\mathbf{e}}_\sigma = (\hat{\mathbf{x}} + i\sigma\hat{\mathbf{y}})/\sqrt{2}$ are the unit vectors for left-handed ($\sigma = 1$) and right-handed ($\sigma = -1$) circular polarizations. More general vortex beams and polarizations can also be analyzed by using the method outlined below.

The strongly focused nonparaxial beam after the objective (obeying the sine condition) is obtained from Eq. (2) as a Debye-type (Fourier) superposition of plane waves [37] with wave vectors $\mathbf{k}(\theta, \varphi)$ spanning the angular sector defined by the conditions $0 \leq \varphi < 2\pi$ and $0 \leq \theta \leq \theta_0 = \sin^{-1}(\frac{NA}{n_i})$, where n_i is the refractive index of glass. All Fourier components satisfy $|\mathbf{k}(\theta, \varphi)| = n_i k_0$.

The focused beam is then further refracted at the interface between the glass slide and the sample region filled with water shown in the inset of Fig. 1. In a typical oil-immersion objective, such refraction has an important effect on the optical force [28] as it degrades the focal region by the introduction of spherical aberration [27]. For each Fourier component, the resulting spherical aberration phase scales with the distance L between the objective focal plane and the slide [35] shown in the inset of Fig. 1:

$$\Phi(\theta) = kL \left(-\frac{\cos\theta}{N_a} + N_a \cos\theta_1 \right), \quad (3)$$

where $\theta_1 = \sin^{-1}(\sin\theta/N_a)$ is the refraction angle in the sample filled with water, and $N_a = n_1/n_i$ is the relative refractive index of water with respect to the glass medium. The resulting electric field in the sample region is then given by

$$\begin{aligned} \mathbf{E}_\ell^{(\sigma)}(\mathbf{r}) &= \left[\frac{-ikf \exp(-ikf)}{2\pi} \right] E_0 (-\sqrt{2}\gamma)^{|\ell|} \\ &\times \int_0^{2\pi} d\varphi \exp(i\ell\varphi) \int_0^{\theta_0} d\theta (\sin\theta)^{1+|\ell|} \\ &\times \sqrt{\cos\theta} \exp(-\gamma^2 \sin^2\theta) T(\theta) \exp[i\Phi(\theta)] \\ &\times \exp[i\mathbf{k}_1(\theta_1, \varphi) \cdot \mathbf{r}] \hat{\mathbf{e}}'_\sigma(\theta_1, \varphi), \end{aligned} \quad (4)$$

where $\gamma = f/w_0$ is the ratio between the objective focal length f and the beam waist at the entrance port, and $\mathbf{k}_1(\theta_1, \varphi)$ is the wave vector in the sample region corresponding to propagation direction (θ_1, φ) . The unit vector $\hat{\mathbf{e}}'_\sigma(\theta_1, \varphi) = (\hat{\mathbf{x}}' + i\sigma\hat{\mathbf{y}}')/\sqrt{2}$ is given in terms of the unit vectors $\hat{\mathbf{x}}'$ and $\hat{\mathbf{y}}'$

obtained from $\hat{\mathbf{x}}$ and $\hat{\mathbf{y}}$ by rotation with Euler angles $(\varphi, \theta_1, -\varphi)$. Additionally, the coefficient

$$T(\theta) = \frac{2 \cos\theta}{\cos\theta + N_a \cos\theta_1} \quad (5)$$

is the Fresnel transmission amplitude for the glass-water interface.

For high-NA objectives, the part of the angular spectrum corresponding to $\theta > \sin^{-1}(N_a)$ gives rise to evanescent waves in the sample region. We assume that the trapped particle is a few wavelengths away from the glass slide at the bottom of the sample region, allowing us to neglect the contribution of the evanescent sector as well as the effect of optical reverberation between particle and glass slide [43]. We discard the contribution from the evanescent sector by taking $\theta_0 = \sin^{-1}(N_a)$ in Eq. (4) when $NA > n_1$.

We compute the Mie scattered field for each component of the angular spectrum of the nonparaxial incident field with the help of the Wigner rotation matrix elements [44] $d_{m,m'}^j(\theta_1)$, allowing us to consider all directions of incidence contained in the spectrum. Finally, the optical force \mathbf{F} is derived from the Maxwell stress tensor. As the former is proportional to the laser beam power P at the sample, we define the dimensionless force [45]:

$$\mathbf{Q} = \frac{\mathbf{F}}{n_1 P/c}, \quad (6)$$

where c is the speed of light in vacuum. The resulting optical force is the sum of two contributions [33]: The extinction term \mathbf{Q}_e represents the rate of linear momentum removal from the incident field. Part of this momentum is carried away by the scattered field at a rate $-\mathbf{Q}_s$. The rate of momentum transferred to the particle is then $\mathbf{Q} = \mathbf{Q}_e + \mathbf{Q}_s$. The cylindrical components are written as a partial-wave series of the form:

$$\sum_{jm} = \sum_{j=1}^{\infty} \sum_{m=-j}^j.$$

The axial extinction contribution reads

$$Q_{ez} = \frac{2(2\gamma^2)^{|\ell|+1}}{|\ell|! A_\ell N_a} \text{Re} \sum_{jm} (2j+1)(a_j + b_j)(G_{j,m} G_{j,m}^*). \quad (7)$$

Here, a_j and b_j are the Mie coefficients for electric and magnetic multipoles [46], respectively, and A_ℓ is the fraction of the trapping beam power that fills the objective entrance port of radius R_p and is refracted into the sample (see Appendix A for details).

The multipole coefficients appearing in Eq. (7) are given by

$$\begin{aligned} G_{jm} &= \int_0^{\theta_0} d\theta (\sin\theta)^{1+|\ell|} \sqrt{\cos\theta} T(\theta) \\ &\times \exp(-\gamma^2 \sin^2\theta) d_{m,1}^j(\theta_1) J_{m-|\ell|}(k\rho \sin\theta_1) \\ &\times \exp[i\Phi(\theta)] \exp(in_1 k_0 \cos\theta_1 z), \end{aligned} \quad (8)$$

$$\begin{aligned} G'_{jm} &= \int_0^{\theta_0} d\theta (\sin\theta)^{1+|\ell|} \sqrt{\cos\theta} \cos\theta_1 T(\theta) \\ &\times \exp(-\gamma^2 \sin^2\theta) d_{m,1}^j(\theta_1) J_{m-|\ell|}(k\rho \sin\theta_1) \\ &\times \exp[i\Phi(\theta)] \exp(in_1 k_0 \cos\theta_1 z), \end{aligned} \quad (9)$$

where J_m are the cylindrical Bessel functions of integer order [47].

The remaining cylindrical components of \mathbf{Q}_e as well as the components of \mathbf{Q}_s are written in a similar way. Explicit expressions can be found in Appendix B.

IV. RESULTS

A. Trapping states for aberration-free systems

For clarity, we first present theoretical results for an aberration-free focused beam, which in principle can be implemented with a water-immersion objective. We then take $N_a = 1$ in Eq. (3) leading to a vanishing spherical aberration phase $\Phi = 0$.

In this case, the electric energy density in the focal region was discussed in Refs. [17–20]. For any nonzero topological charge, it has the shape of a ring that depends on the relative sign between ℓ and σ . On the focal plane, the peak electric energy density is at a distance \tilde{r}_ℓ from the axis, which was shown to scale linearly with ℓ for a fixed waist w_0 when $\ell \gg 1$ [20,24], whereas the radius of the paraxial vortex beam r_ℓ scales with $\sqrt{\ell}$ as shown in Eq. (1). The variation of \tilde{r}_ℓ with ℓ and r_ℓ/R_p (defining how the vortex beam fills the objective entrance port of radius R_p) is discussed in detail in Appendix A. For all numerical results presented in the present subsection, we take the value $r_\ell/R_p = 0.8$, which provides a diffraction limited spot with a relatively small power loss as discussed in Appendix A. We also take $n_1 = 1.332$ and $n_2 = 1.576$ for the refractive indexes of water and polystyrene, respectively.

Two trapping regimes are expected depending on the comparison between the microsphere radius a and the characteristic size \tilde{r}_ℓ of the focal spot [7,25,26]. When $a \ll \tilde{r}_\ell$, the particle is trapped near the ring of maximum energy density while being driven by the optical torque [23,24]. This is in line with the simple Rayleigh picture of an optical force proportional to the gradient of the electric energy density, alongside a nonconservative force component that drives the particle around the beam axis. In the opposite limit of radius $a \gg \tilde{r}_\ell$, the microsphere is trapped on the optical axis as it is too big to resolve the spatial variation of the annular focal spot.

Our Mie-Debye results presented below confirm the existence of these two trapping regimes. More importantly, we find that, at intermediate particle sizes $a \sim \tilde{r}_\ell$, the two stable trapping states coexist. In this case, the particle might randomly hop between the on-axis position and the annular focal spot by thermal activation provided that the laser beam power is sufficiently low.

For on-axis trapping, it is required that the radial trap stiffness satisfies $\kappa_\rho = -(n_1 P/c)(\partial Q_\rho/\partial \rho)|_{\rho=0} > 0$. We first compute the stable axial position z_{eq} by solving $Q_z(\rho = 0, z_{\text{eq}}) = 0$ and then calculate the numerical derivative of the function $Q_\rho(\rho, z_{\text{eq}})$ at $\rho = 0$. In Fig. 2, we show the variation of κ_ρ/P with microsphere radius for different values of ℓ . For any positive value of ℓ , we find that κ_ρ changes its sign from negative to positive at a critical sphere radius R_{on} that increases with ℓ . Thus, on-axis trapping is excluded for sphere radii smaller than R_{on} . Particles in this size range are trapped on the annular region and are driven by the optical torque. In line with the previous qualitative discussion, R_{on} is

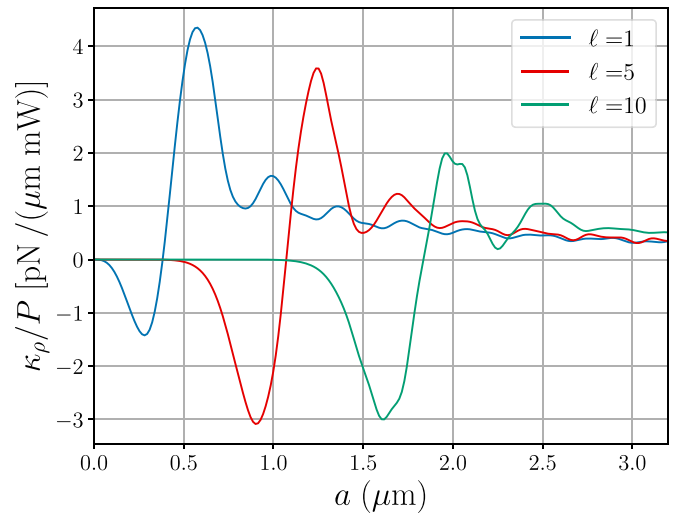


FIG. 2. Transverse trap stiffness per unit power κ_ρ/P as a function of the sphere radius for topological charges $\ell = 1$ (blue), 5 (red), and 10 (green). We consider an aberration-free trapping beam. As the particle size increases, κ_ρ changes sign from negative to positive at the critical radius R_{on} .

comparable with the focal spot annular radius \tilde{r}_ℓ . Indeed, we plot R_{on} (green) and \tilde{r}_ℓ (circles) as functions of ℓ in Fig. 3, showing that R_{on} is slightly smaller than \tilde{r}_ℓ . In the region below the line defined by R_{on} in Fig. 3, trapping occurs on the annular region only.

The condition for off-axis trapping defines a second critical radius R_{off} . When $a > R_{\text{off}}$, off-axis trapping is excluded as the only root of $Q_\rho(\rho, z = 0) = 0$ is at $\rho = 0$, with $Q_\rho(\rho, z = 0) < 0$ for any $\rho > 0$. In Fig. 3, we plot the variation of R_{off} with ℓ (blue). Here, R_{off} is very close to \tilde{r}_ℓ for small values of ℓ and then becomes increasingly larger than \tilde{r}_ℓ as ℓ increases.

On- and off-axis stable equilibria coexist between the two exclusion zones shown in Fig. 3, corresponding to microsphere radii in the (colored) stripe defined by $R_{\text{on}} < a < R_{\text{off}}$. Depending on the optical potential landscape, which scales with the laser beam power, a bistable trap might be demonstrated in this case by measuring the thermally activated hopping between the two mesostates.

As an illustration of the different trapping regimes, we plot $Q_\rho(\rho, z = 0)$ vs ρ in Fig. 4 for three different microsphere radii: $a = 1.5 \mu\text{m}$ (blue), $2.25 \mu\text{m}$ (red), and $3.5 \mu\text{m}$ (green). In all cases, we take $\ell = 11$, for which we find $R_{\text{on}} = 2.0 \mu\text{m}$ and $R_{\text{off}} = 2.3 \mu\text{m}$. Thus, the three radii considered in Fig. 4 illustrate the three trapping regimes defined by the parameter space shown in Fig. 3. For the smallest size, Fig. 4 shows that the axial equilibrium position is unstable, in agreement with the results shown in Fig. 2, whereas the positive root of $Q_\rho(\rho) = 0$ corresponds to stable equilibrium. For the largest particle, the only (stable) equilibrium position is at $\rho = 0$, whereas for the intermediate size two stable equilibria are shown.

For further insight, we also show in Fig. 4 the electric energy density as a function of ρ (fill plot). The edge of a microsphere with $a = 1.5 \mu\text{m}$ is located near the inner tail of the electric energy density distribution when its center is aligned along the axis. As it would sit almost entirely on the

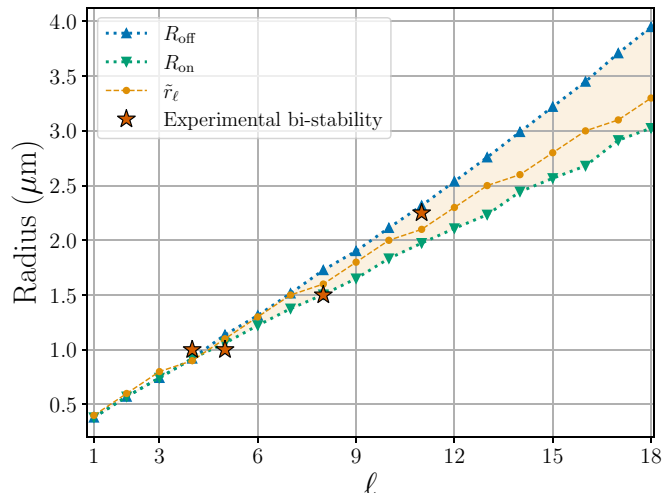


FIG. 3. For an aberration-free trapping beam, the parameter space spanned by the microsphere radius and the topological charge ℓ is divided into three different regions. For radii smaller than the critical radius $R_{\text{on}}(\ell)$ (green), on-axis trapping is excluded, and the particle rotates around the optical axis along a circular trajectory. For radii larger than the critical radius $R_{\text{off}}(\ell)$ (blue), orbital trapping is excluded, and the particle is trapped at a position along the optical axis. On-axis and orbital states coexist in the (colored) bistable stripe bounded by the plots of $R_{\text{on}}(\ell)$ and $R_{\text{off}}(\ell)$. Such a region corresponds to radii close to the maximum of electric energy density \tilde{r}_ℓ (circle). When an oil-immersion objective is employed, the spherical aberration introduced by refraction at the glass slide opens the way to switch between trapping regimes by changing the height L of the objective focal plane. However, experimental bistability is possible only for radii and topological charges (red stars) close to or within the orange colored stripe.

dark central part of the annular spot, stable on-axis equilibrium is indeed not possible in this case. On the other hand, a microsphere with $a = 3.5 \mu\text{m}$ encompasses the entire bright annulus when placed on axis, which is consistent with stable on-axis trapping. Finally, the intermediate size microsphere ($a = 2.25 \mu\text{m}$), for which a bistable behavior is predicted, is such that its edge nearly coincides with the energy density

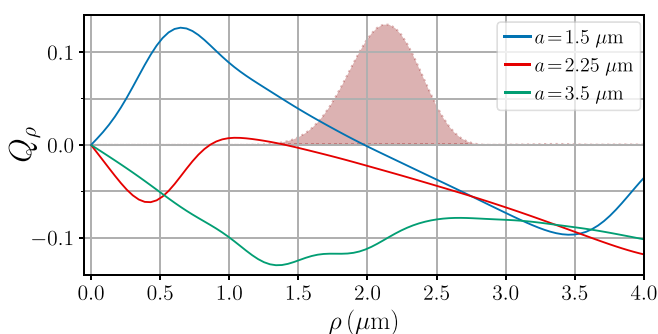


FIG. 4. Radial optical force component Q_ρ as a function of radial position ρ for $\ell = 11$ and radii $a = 1.5 \mu\text{m}$ (blue), $a = 2.25 \mu\text{m}$ (red), and $a = 3.5 \mu\text{m}$ (green). The fill plot indicates the electric energy density variation with distance to the optical axis. Its maximum is located at $\tilde{r}_\ell = 2.1 \mu\text{m}$

TABLE I. Experimental values for the radius ρ_{exp} and period T_{exp} of the orbit when the microsphere is off-axis [see Figs. 5(b) and 5(c)] in the bistable regime for given values of the topological charge ℓ , particle radius a , and power at the entrance port P_{port} . The theoretical values for the radius of the orbit ρ_{theo} are in good agreement with the experimental data for $\ell = 5$ and 8, but for $\ell = 4$, only on-axis trapping is predicted by the model.

ℓ	a (μm)	P_{port} (mW)	ρ_{theo} (μm)	ρ_{exp} (μm)	T_{exp} (s)
4	1.0	56 ± 1	—	0.6 ± 0.1	0.24 ± 0.02
5	1.0	56 ± 1	0.69 ± 0.01	0.7 ± 0.2	0.20 ± 0.01
8	1.5	65 ± 1	1.07 ± 0.01	1.0 ± 0.2	0.55 ± 0.03
11	2.25	62 ± 1	1.2 ± 0.1	1.9 ± 0.3	5 ± 1

peak at $\rho = \tilde{r}_\ell$. Such a discussion indicates that the width of the bistable stripe in the parameter space of Fig. 3 scales with the width of the focal spot annular region. As the latter increases with ℓ , we expect the bistable stripe to become wider as ℓ increases, which is indeed in agreement with the results shown in Fig. 3.

B. Experimental demonstration of bistability by tuning the spherical aberration

For a typical optical tweezers setup employing an oil-immersion objective, the spherical aberration phase in Eq. (3) introduced by refraction of the trapping beam at the glass-water interface brings in the height L of the focal plane (see Fig. 1) as a third parameter that adds to the microsphere radius and topological charge to form a richer parameter space. Experimentally, L can be finetuned by displacing the sample with the help of a piezoelectric nanopositioning stage as discussed in Sec. II. In the present subsection, we show that spherical aberration provides indeed a useful tool for demonstrating a bistable trap and, more generally, for switching between different trapping states for fixed values of particle size and topological charge.

Although the results of Fig. 3 do not consider spherical aberration, they still provide a useful guide for achieving bistability with our experimental setup employing an oil-immersion objective. Indeed, we can experimentally demonstrate a thermally activated bistable trapping by finetuning the height L and employing moderate laser powers when taking particles of radius a illuminated by vortex beams of charge ℓ close to the bistable stripe shown in Fig. 3 but not otherwise. The stars in Fig. 3 indicate the experimental implementations of bistability. The corresponding values of ℓ , a , and the laser beam power P_{port} at the objective entrance port allowing for bistability are shown in Table I. In all of those cases, we start by trapping the microsphere on the axis with the focal plane close to the glass slide and then increase the height L by displacing the sample downwards. As L increases, we first switch from axial to bistable trapping and then from bistable to off-axis orbital motion (see the Supplemental Material [48]).

A typical bistable trapping is obtained for $\ell = 8$ and $a = 1.5 \mu\text{m}$ by displacing the sample downward by $d = 2 \mu\text{m}$ with respect to the initial position, leading to axial trapping. Then

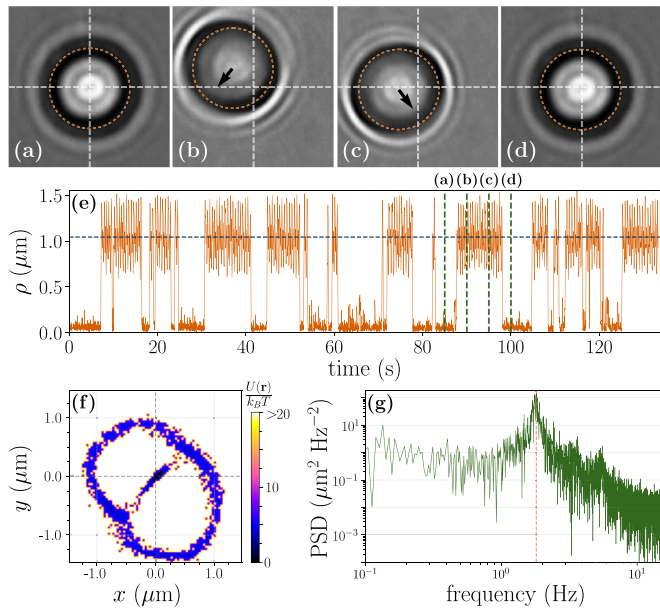


FIG. 5. Experimental realization of bistability with a polystyrene microsphere of radius $a = 1.5 \mu\text{m}$ and a vortex beam with $\ell = 8$. (a)–(d) show frames of the trapped microsphere at times $t_{(a)} = 85 \text{ s}$, $t_{(b)} = 90 \text{ s}$, $t_{(c)} = 95 \text{ s}$, and $t_{(d)} = 100 \text{ s}$. The outline (dash) of the trapped microsphere of diameter $a = 3 \mu\text{m}$ is superimposed on each image to represent the scale. When the microsphere hops to an off-axis location (b) and (c), it circulates around the axis. The black arrows indicate the direction of motion in (b) and (c). The difference between the image patterns in (a) and (d) and in (c) and (d) indicates that the trapping height changes when hopping from axial equilibrium to orbital motion. (e) Time series for the radial coordinate. The vertical green lines indicate the times corresponding to the frames shown in (a)–(d). The horizontal dashed line represents the mean radial coordinate $\rho_{\text{exp}} = (1.04 \pm 0.05) \mu\text{m}$ for the orbital state. (f) Color map of the energy distribution $U(x, y)/(k_B T)$ across the xy plane as derived from the position distribution density $p(x, y)$. (g) Power spectrum density (PSD) of the x coordinate showing a peak at $f = 1.82 \text{ Hz}$, which corresponds to an orbital period $T_{\text{exp}} = (0.55 \pm 0.03) \text{ s}$.

a second displacement by the same amount leads to off-axis orbital trapping.

The experimental results for the intermediate configuration leading to bistability are summarized in Fig. 5. Panels (a)–(d) show frames of the trapped particle as it hops from the axial position (a) to the off-axis orbit (b) and (c) and back (d). Note that the orbital motion blurs the diffraction rings along the direction of displacement (black arrow) in the image patterns shown in panels (b) and (c). The clear difference between image patterns in (a) and (d) for on-axis trapping and in (b) and (c) for orbital motion indicates [49] that these two mesostates correspond to different heights, which is confirmed by the theoretical discussion presented in the next subsection.

The alternation between on- and off-axis states over time is presented in more detail in Fig. 5(e), where we plot the microsphere radial position ρ vs time. We determine the radius of the orbit ρ_{exp} from the average (horizontal dashed line) and the standard error of ρ in the orbital state. The resulting figures for $\ell = 8$ as well as for the other values of ℓ are indicated in

Table I. The instants of time corresponding to panels (a)–(d) are indicated in panel (e) as vertical dashed lines. The complete trajectory is captured by 4000 frames, corresponding to a total time 133 s, from which we determine the position probability distribution $p(x, y)$ on the xy plane by taking bins of area $\Delta x \Delta y = 1.35 \times 10^{-3} \mu\text{m}^2$. Subsequently, $p(x, y)$ defines the energy distribution $U(x, y)/(k_B T) = \ln p(0, 0) - \ln p(x, y)$ depicted in panel (f).

In addition to the probability distribution, we also analyze the power spectrum density (PSD) for the x coordinate of the microsphere position [Fig. 5(g)]. A very similar result for the y coordinate is obtained (not shown). The PSD has the form of a superposition of squared sinc functions centered at the orbital frequency $f_{\text{exp}} = 1/T_{\text{exp}}$ (T_{exp} = period of the orbit) and with different widths as determined by the total time elapsed in each orbital motion before hopping back to the axial trapping position. The period T_{exp} is then obtained from the peak of the PSD as indicated in Fig. 5(g). The resulting values are shown in Table I, with the errors bars derived from the half width at half maximum.

As a final remark concerning our experimental results, we note that we find, in all cases, that the sense of rotation coincides with the sign of ℓ . This is also the case of a previous experiment with a vortex beam focused into an aqueous solution [24], but a negative optical torque was predicted for the orbital motion in air [50]. A negative torque was also demonstrated for a particle trapped on axis by a circularly polarized Gaussian beam [42]. Our theoretical description of the experiment with vortex beams also confirms that the sense of rotation coincides with the sign of the topological charge. A detailed theory-experiment comparison is presented in the next subsection.

C. Theoretical results with spherical aberration and comparison with experiment

In the present subsection, we derive theoretical results within the MDSA approach developed in Sec. III, taking parameters corresponding to the experiment discussed above. In contrast with Sec. IV A, we now consider the effect of spherical aberration introduced by the glass slide interface, as required for comparison with our experimental results. Indeed, when focusing a laser beam through the glass-water interface, the optical force field is considerably modified by spherical aberration, as shown in the case of a Gaussian beam, for which multiple equilibria were found [28,35]. Note that a focused Gaussian beam contains paraxial Fourier components for which the spherical aberration effect is weaker. Thus, a stronger modification of trapping conditions is expected when focusing a vortex beam overfilling a high-NA objective since the entire angular spectrum is nonparaxial in this case. Here, our primary goal is to understand how spherical aberration controls the onset of bistability.

In Fig. 6(a), we plot the electric energy density and optical force components for different values of L , taking $\ell = 8$ and $a = 1.5 \mu\text{m}$. The columns correspond to the three positions of the objective focal plane with respect to the glass slide employed in the experiment, with the leftmost one depicting trapping closer to the slide. From left to right, we displace the focal plane by steps of $\Delta L = N_a d = 1.75 \mu\text{m}$, thus

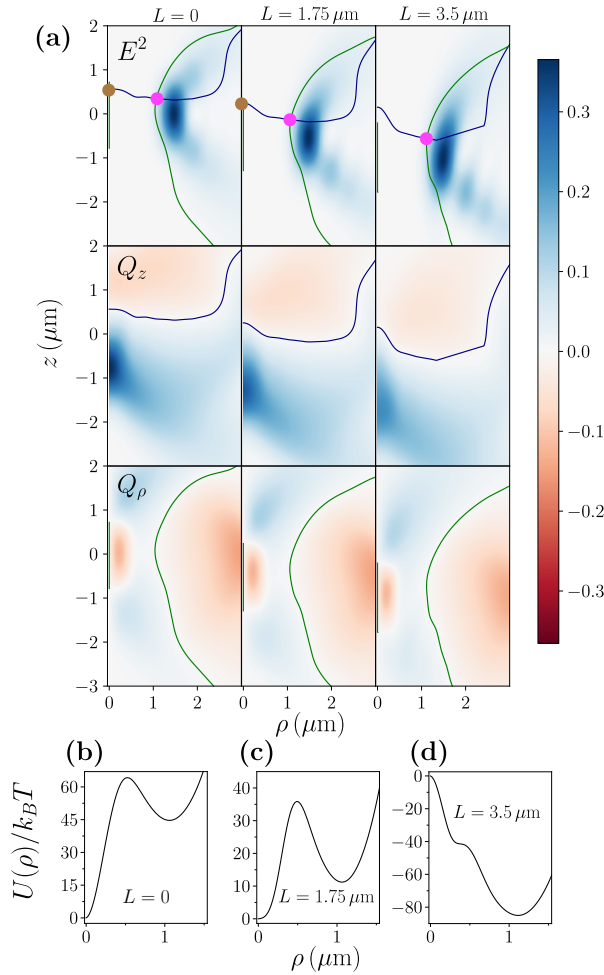


FIG. 6. Theoretical results for the variation of the optical force field with spherical aberration. The distance L between the objective focal plane (for paraxial rays) and the glass slide is increased from left to right, thus enhancing the spherical aberration introduced by refraction at the interface between the slide and the sample. We consider a vortex beam with $\ell = 8$ and left-handed circular polarization ($\sigma = +1$) at the objective entrance port and a polystyrene microsphere with radius $a = 1.5 \mu\text{m}$. (a) From top to bottom, density plots representing the electric energy density E^2 and the axial and radial force components Q_z and Q_ρ , respectively, on a meridional plane. The force components are normalized by Eq. (6) and their values are indicated by the color bar. The roots of $Q_z = 0$ (blue line) and $Q_\rho = 0$ (green line) as well as the positions of axial (brown dot) and orbital (magenta dot) stable equilibria are also indicated. Optical potential (in units of the thermal energy $k_B T$) vs radial distance ρ for (b) $L = 0 \mu\text{m}$, (c) $L = 1.75 \mu\text{m}$, and (d) $L = 3.5 \mu\text{m}$.

mimicking the experimental procedure outlined in the previous subsection. The density plots represent the electric energy density E^2 and the axial (Q_z) and radial (Q_ρ) optical force components as functions of the microsphere position in cylindrical coordinates. The plane $z = 0$ corresponds to the laser paraxial focal plane. By symmetry, E^2 , Q_z , and Q_ρ are independent of ϕ .

The electric energy density depicted in the first line of Fig. 6(a) spreads out radially and into the region below the laser paraxial focal plane as a result of the increase

of the spherical aberration phase in Eq. (3). The density plots of the optical force components allow us to identify the roots of $Q_\rho = 0$ and $Q_z = 0$ leading to stable trapping. They are indicated as green and blue lines, respectively. The equilibrium configurations are obtained as the intersections between the two lines in Fig. 6(a), which are indicated as brown and magenta dots for axial and orbital trapping states, respectively.

In the absence of spherical aberration ($L = 0$), the green and blue lines intersect at an axial position as well as off axis, in line with the result of Fig. 3 since the parameters ($\ell = 8$, $a = 1.5 \mu\text{m}$) lie within the bistable colored region. To understand why the microsphere stays on the axis in this case, we plot in Fig. 6(b) the corresponding optical potential $U(\rho) \equiv -\int_0^\rho F_\rho[\rho, \bar{z}(\rho)]d\rho$, where $\bar{z}(\rho)$ is the axial coordinate leading to a vanishing axial force at ρ : $Q_z[\rho, \bar{z}(\rho)] = 0$ [the function $\bar{z}(\rho)$ corresponds to the blue lines in Fig. 6(a)]. To calculate the radial force component F_ρ , we consider the expressions for Q_ρ given in Appendix B and determine the power at the sample $P = 3.8 \text{ mW}$ from the period of rotation (see Appendix C for details). Since the conservative component of the optical force field is given as the negative gradient of the optical potential, the latter contains all the information required for the discussion of the relative stability between different trapping states. On the other hand, the nonconservative component brings crucial information about the nature of the different states. The azimuthal force component drives the microsphere along the NESS orbit for the off-axis state.

Figure 6(b) indicates that the well at $\rho = 0$ is much deeper than the one corresponding to off-axis orbital motion, which explains the experimental observation of stable axial trapping in the absence of spherical aberration ($L = 0$). As L increases, the off-axis well gets deeper, leading to the bistable trapping near $L = 1.75 \mu\text{m}$ [Fig. 6(c)]. When compared with the experimental energy distribution shown in Fig. 5(f), theory overestimates the difference between the local minima by a factor ~ 2 . Note that the energy difference between the two minima shown in Fig. 6(c) is proportional to the power P_{port} at the entrance port. We observe, experimentally, that the bistable behavior disappears as the power increases, with the sphere remaining on axis, in agreement with the theoretical result that the potential energy minimum at $\rho = 0$ is lower than the off-axis one in Fig. 6(c). On the other hand, off-axis orbital trapping is favored by further increasing L . Indeed, the theoretical potential for $L = 3.5 \mu\text{m}$ shown in Fig. 6(d) shows that the axial equilibrium position eventually disappears as the focal spot continues to spread out by increasing L , which is in line with experimental observation and with the absence of intersection between the green and red lines shown in Fig. 6(a).

Figure 6(a) clearly indicates that the two mesostates in the bistable regime ($L = 1.75 \mu\text{m}$) correspond to different heights. Indeed, the vertical distance between the brown and magenta dots in the corresponding panel of Fig. 6(a) gives $\Delta z = z_{\text{axis}} - z_{\text{orb}} 0.3 \mu\text{m}$, which is consistent with the image patterns shown in Figs. 5(a)–5(d).

Figure 5(f) shows that the distribution $p(x, y)$ near the axis is elongated along the direction bisecting the first and third quadrants of the xy plane, while the orbit is extended along the

orthogonal direction. Similar shapes are found for the other values of ℓ shown in Table I. Those properties are consistent with astigmatism of the trapping beam [41,51], with the plane of least confusion located between the planes of the orbital motion and of the on-axis equilibrium discussed in the previous paragraph. Figure 5(f) also indicates that astigmatism plays an important role in the transitions between axial and orbital states. Indeed, the position distribution shows that the particle preferably hops to and from orbital microstates closer to the axial state. Such bias is not captured by our stigmatic model, which requires unbiased thermal fluctuations to break the rotational symmetry when hopping from the axial state to a given microstate along the circular orbit. When compared with the potential landscape calculated for our axially symmetric stigmatic model shown in Fig. 6(c), the potential barrier between the axial state and the orbital microstates closer to the axis should be reduced by astigmatism, thus facilitating thermally activated hops along both ways as observed in the experiment.

The theoretical results for the orbital radii are organized in Table I, with the errors arising from the uncertainty of L . Although our model does not consider astigmatism, we still find good agreement with the experimental data for $\ell = 5$ and 8. Indeed, it is generally expected that particles with radii $a > \lambda_0$ average out the imperfections arising from astigmatism [41]. However, λ_0 is replaced by the radius of the annular spot $\tilde{r}_\ell > \lambda_0$ as the characteristic size of the diffraction-limited focal spot when employing vortex beams. Thus, we attribute the agreement mostly to time averaging the radial distance over several periods of revolution, which effectively averages out the elongation of the orbit shown in Fig. 5(f).

For $\ell = 4$, our theoretical model predicts axial trapping only, regardless of the amount of spherical aberration. In other words, in this case, the prediction of stable axial trapping with an aplanatic focused beam [note that $a = 1.0 \mu\text{m} > R_{\text{off}}(\ell = 4)$ as indicated in Fig. 3] is not modified by the introduction of spherical aberration.

V. CONCLUSION

In conclusion, we have demonstrated bistable optical trapping by employing a vortex beam at the objective back aperture. The NESS corresponding to orbital motion driven by the optical torque coexists with stable axial trapping. The corresponding bistable optical potential has the form of a Mexican hat with an additional minimum at its center. To achieve such bistable trapping, the microsphere diameter should be comparable with the diameter of the laser focal spot, which has an annular shape in the case of circular polarization.

Our experimental results are compared with an extension of MDSA theory of optical tweezers considering a circularly polarized vortex beam at the objective back aperture. The ideal case of an aplanatic focused beam provides a useful guide in the search for bistable behavior. It shows that the range of particle sizes yielding bistability becomes wider as the topological charge increases. However, spherical aberration is essential for a full description of our experiment employing an oil-immersion objective. More importantly, spherical aberration allows us to tailor different trapping regimes. Indeed, since the focal height can be precisely

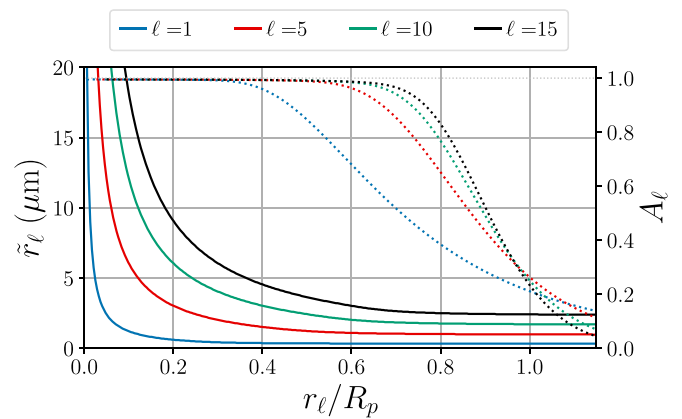


FIG. 7. Radius \tilde{r}_ℓ of the focal annular spot (solid, left axis) and filling factor A_ℓ representing the fraction of total power transmitted to the sample chamber (dot, right axis) as functions of the radius r_ℓ of the paraxial vortex beam (in units of the objective entrance radius $R_p = 2.8 \text{ mm}$). The topological charges are $\ell = 1, 5, 10$, and 15. We consider an oil-immersion objective lens with numerical aperture $\text{NA} = 1.4$.

controlled with the help of a piezoelectric nanopositioning system, our system allows us to manipulate the transition from a single state, either on the optical axis or in a well-defined orbit, to a metastable state. The cyclic hops between the two mesostates, each with a significantly distinct set of microstates, open the way for investigating the energetics of cyclic symmetry breaking and restoration [30]. The possibility of employing a time-dependent focal height could also find applications in shortcuts to equilibration [52–54] connecting mesostates with different symmetries.

ACKNOWLEDGMENTS

We are grateful to C. S. Nascimento, C. Genet, F. Impens, G.-L. Ingold, R. Goerlich, and T. Schoger for fruitful discussions. A.L.F. expresses his deepest gratitude to the Light-matter Interactions and Nanostructures group at Institut de Science et d'Ingénierie Supramoléculaire (ISIS, Strasbourg, France) for their hospitality during his stay as a visiting student. P.A.M.N. acknowledges funding from the Brazilian agencies Conselho Nacional de Desenvolvimento Científico e Tecnológico (CNPq–Brazil), Coordenação de Aperfeiçoamento de Pessoal de Nível Superior (CAPES–Brazil), Instituto Nacional de Ciência e Tecnologia de Fluidos Complexos (INCT-FCx), and the Research Foundations of the States of Rio de Janeiro (FAPERJ) and São Paulo (FAPESP).

APPENDIX A: OBJECTIVE FILLING

Objective filling conditions are particularly important when using a vortex beam, as we need to optimize the energy density gradient (by reducing the size of the focal spot) while keeping most of the annular section of the incoming beam inside the objective entrance port. Filling is controlled by the ratio r_ℓ/R_p between the radius of the vortex beam r_ℓ , given by Eq. (1), and the radius of the objective entrance port R_p .

TABLE II. Vortex beam waist w_0 and ratio between the radii of the beam (at the objective entrance port) and of the objective entrance port $R_p = (2.80 \pm 0.05)$ mm.

ℓ	a (μm)	w_0 (mm)	r_ℓ/R_p
4	1.0	1.78 ± 0.02	0.90 ± 0.01
5	1.0	1.83 ± 0.02	1.03 ± 0.01
8	1.5	0.95 ± 0.01	0.68 ± 0.01
11	2.25	0.89 ± 0.01	0.74 ± 0.01

In Fig. 7, we plot the radius \tilde{r}_ℓ of the focal annular spot (solid) and the filling factor A_ℓ (dot), with

$$A_\ell = \frac{8(2\gamma^2)^{|\ell|+1}}{|\ell|!} \int_0^{\sin\theta_0} ds s^{2|\ell|+1} \exp[-2(\gamma s)^2] \times \frac{\sqrt{(1-s^2)(N_a^2-s^2)}}{(\sqrt{1-s^2} + \sqrt{N_a^2-s^2})^2}, \quad (\text{A1})$$

as functions of r_ℓ/R_p for different values of ℓ . We consider the oil-immersion objective used in the experiment (see Sec. II for details).

As expected, the fraction of the total power that enters the objective entrance port decreases as the radius of

the vortex beam r_ℓ increases. The focal spot radius \tilde{r}_ℓ also decreases with r_ℓ/R_p , reaching diffraction-limited values (which scale linearly with ℓ [20,24]) at $r_\ell/R_p \gtrsim 0.8$. To simulate a diffraction-limited spot with the minimal power loss, we take $r_\ell/R_p = 0.8$ for the aberration-free calculations presented in Sec. IV A. The values of r_ℓ/R_p corresponding to the experiment, shown in Table II, are employed for the calculation of the MDSA results which are compared with the experimental data.

To stay close to the optimal filling condition, we produce vortex beams with increasingly smaller values of the waist w_0 as ℓ increases, as indicated in Table II. Such a condition also allows the vortex beam to develop a finite curvature as it propagates toward the objective back aperture. The resulting curvature of field shifts the whole laser focal spot upward without changing the amount of spherical aberration [39], thus making room for trapping above the glass slide despite the small values of the objective focal height L employed in the experiment.

APPENDIX B: PARTIAL-WAVE (MULTIPOLE) SERIES FOR THE OPTICAL FORCE CYLINDRICAL COMPONENTS

The radial and azimuthal components of the extinction contribution to the optical force are given by

$$Q_{e\rho} = \frac{(2\gamma^2)^{|\ell|+1}}{|\ell|!A_\ell N_a} \text{Im} \sum_{jm} \{(2j+1)(a_j + b_j)G_{j,m}[G_{j,m+1}^{(-)} - G_{j,m-1}^{(+)}]^*\}, \quad (\text{B1})$$

$$Q_{e\phi} = \frac{-(2\gamma^2)^{|\ell|+1}}{|\ell|!A_\ell N_a} \text{Re} \sum_{jm} \{(2j+1)(a_j + b_j)G_{j,m}[G_{j,m+1}^{(-)} + G_{j,m-1}^{(+)}]^*\}. \quad (\text{B2})$$

Here, we have defined the additional coefficients:

$$G_{jm}^\pm = \int_0^{\theta_0} d\theta (\sin\theta)^{1+|\ell|} \sqrt{\cos\theta} \sin\theta_1 \exp(-\gamma^2 \sin^2\theta) T(\theta) d_{m\pm 1,1}^j(\theta_1) J_{m-1-\ell}(k\rho \sin\theta_1) \exp[i\Phi(\theta)] \exp(in_1 k_0 \cos\theta_1 z). \quad (\text{B3})$$

Finally, the scattering contribution to the optical force is written in terms of cylindrical components as follows:

$$Q_{s\rho} = \frac{2(2\gamma^2)^{|\ell|+1}}{|\ell|!A_\ell N_a} \sum_{jm} \left\{ \frac{\sqrt{j(j+2)(j+m+1)(j+m+2)}}{(j+1)} \text{Im}[(a_j a_{j+1}^* + b_j b_{j+1}^*)(G_{j,m} G_{j+1,m+1}^* + G_{j,-m} G_{j+1,-m-1}^*)] - 2 \frac{(2j+1)}{j(j+1)} \sqrt{(j-m)(j+m+1)} \text{Re}(a_j b_j^*) \text{Im}(G_{j,m} G_{j,m+1}^*) \right\}, \quad (\text{B4})$$

$$Q_{s\phi} = \frac{-2(2\gamma^2)^{|\ell|+1}}{|\ell|!A_\ell N_a} \sum_{jm} \left\{ \frac{\sqrt{j(j+2)(j+m+1)(j+m+2)}}{(j+1)} \text{Re}[(a_j a_{j+1}^* + b_j b_{j+1}^*)(G_{j,m} G_{j+1,m+1}^* - G_{j,-m} G_{j+1,-m-1}^*)] - 2 \frac{(2j+1)}{j(j+1)} \sqrt{(j-m)(j+m+1)} \text{Re}(a_j b_j^*) \text{Re}(G_{j,m} G_{j,m+1}^*) \right\}, \quad (\text{B5})$$

$$Q_{sz} = \frac{-4(2\gamma^2)^{|\ell|+1}}{|\ell|!A_\ell N_a} \sum_{jm} \left\{ \frac{\sqrt{j(j+2)(j-m+1)(j+m+1)}}{(j+1)} \times \text{Re} \left[(a_j a_{j+1}^* + b_j b_{j+1}^*)(G_{j,m} G_{j+1,m}^*) + \frac{(2j+1)}{j(j+1)} m (a_j b_j^*)(G_{j,m} G_{j,m}^*) \right] \right\}. \quad (\text{B6})$$

APPENDIX C: LASER POWER IN THE SAMPLE REGION

Due to the nonuniform transmittance [55] of our high-NA objective, we were not able to estimate the laser power P delivered to the sample from the power at the objective entrance port. Instead, we determine P from the period of rotation T_{exp} by taking the Stokes friction force along the orbital motion to match the azimuthal component of the optical force: $\beta v_{\phi} = n_1 P Q_{\phi} / c$, where $v_{\phi} = 2\pi \rho_{\text{exp}} / T_{\text{exp}}$ is the velocity along the orbit. The MDSA multipole expansion for Q_{ϕ} is given by Eqs. (B2) and (B5). We take Faxén's correction arising from the glass slide when evaluating the drag coefficient β [56,57]:

$$\beta = \frac{6\pi\eta a}{1 - \frac{9}{16}\left(\frac{a}{h}\right) + \frac{1}{8}\left(\frac{a}{h}\right)^3 - \frac{45}{256}\left(\frac{a}{h}\right)^4 - \frac{1}{16}\left(\frac{a}{h}\right)^5}, \quad (\text{C1})$$

where h is the height of the microsphere center with respect to the glass slide and $\eta = (0.91 \pm 0.02) \text{ mPa s}$ is the viscosity of water at room temperature (298 K).

To estimate h , we start each experimental run with a reference configuration such that the trapped microsphere is barely touching the glass slide. We then displace the sample downward by a distance $d = 2 \mu\text{m}$. Neglecting the variation of the axial trapping position with respect to the laser focal plane, we have $h = a + N_{ad}$. For $\ell = 8$ and $a = 1.5 \mu\text{m}$, we find $\beta = (30 \pm 1) \mu\text{g/s}$ from Eq. (C1). The azimuthal optical force is given by $Q_{\phi} = 0.0212$, and then the resulting power is $P = 3.8 \text{ mW}$. When compared with the power P_{port} at the objective entrance port given in Table I, we note that the objective transmittance for the vortex beam overfilling the objective is indeed much smaller than typical values for Gaussian beams, in agreement with the results of Ref. [55].

-
- [1] A. Ashkin, J. M. Dziedzic, J. E. Bjorkholm, and S. Chu, Observation of a single-beam gradient force optical trap for dielectric particles, *Opt. Lett.* **11**, 288 (1986).
- [2] A. Ashkin, *Optical Trapping and Manipulation of Neutral Particles Using Lasers: A Reprint Volume with Commentaries* (World Scientific, Singapore, 2006).
- [3] A. Gennerich, *Optical Tweezers: Methods and Protocols*, Methods in Molecular Biology (Springer, New York, 2016).
- [4] A. Forbes, M. de Oliveira, and M. R. Dennis, Structured light, *Nat. Photon.* **15**, 253 (2021).
- [5] H. Rubinsztein-Dunlop, A. Forbes, M. V. Berry, M. R. Dennis, D. L. Andrews, M. Mansuripur, C. Denz, C. Alpmann, P. Banzer, T. Bauer *et al.*, Roadmap on structured light, *J. Opt.* **19**, 013001 (2017).
- [6] Y. Shen, X. Wang, Z. Xie, C. Min, X. Fu, Q. Liu, M. Gong, and X. Yuan, Optical vortices 30 years on: OAM manipulation from topological charge to multiple singularities, *Light Sci. Appl.* **8**, 90 (2019).
- [7] Y. Yang, Y.-X. Ren, M. Chen, Y. Arita, and C. Rosales-Guzmán, Optical trapping with structured light: A review, *Adv. Photon.* **3** (2021).
- [8] M. Li, S. Yan, Y. Zhang, X. Chen, and B. Yao, Optical separation and discrimination of chiral particles by vector beams with orbital angular momentum, *Nanoscale Adv.* **3**, 6897 (2021).
- [9] V. Bobkova, J. Stegemann, R. Droop, E. Otte, and C. Denz, Optical grinder: Sorting of trapped particles by orbital angular momentum, *Opt. Express* **29**, 12967 (2021).
- [10] R. J. C. Spreeuw, Spiraling light: From donut modes to a magnus effect analogy, *Nanophoton.* **11**, 633 (2022).
- [11] L. Allen, M. W. Beijersbergen, R. J. C. Spreeuw, and J. P. Woerdman, Orbital angular momentum of light and the transformation of Laguerre-Gaussian laser modes, *Phys. Rev. A* **45**, 8185 (1992).
- [12] H. He, M. E. J. Friese, N. R. Heckenberg, and H. Rubinsztein-Dunlop, Direct observation of transfer of angular momentum to absorptive particles from a laser beam with a phase singularity, *Phys. Rev. Lett.* **75**, 826 (1995).
- [13] N. B. Simpson, K. Dholakia, L. Allen, and M. J. Padgett, Mechanical equivalence of spin and orbital angular momentum of light: An optical spanner, *Opt. Lett.* **22**, 52 (1997).
- [14] K. Y. Bliokh, E. A. Ostrovskaya, M. A. Alonso, O. G. Rodríguez-Herrera, D. Lara, and C. Dainty, Spin-to-orbital angular momentum conversion in focusing, scattering, and imaging systems, *Opt. Express* **19**, 26132 (2011).
- [15] K. Y. Bliokh, F. J. Rodríguez-Fortuño, F. Nori, and A. V. Zayats, Spin-orbit interactions of light, *Nat. Photon.* **9**, 796 (2015).
- [16] V. V. Kotlyar, A. G. Nalimov, A. A. Kovalev, A. P. Porfired, and S. S. Stafeev, Spin-orbit and orbit-spin conversion in the sharp focus of laser light: Theory and experiment, *Phys. Rev. A* **102**, 033502 (2020).
- [17] D. Ganic, X. Gan, and M. Gu, Focusing of doughnut laser beams by a high numerical-aperture objective in free space, *Opt. Express* **11**, 2747 (2003).
- [18] N. Bokor, Y. Iketaki, T. Watanabe, and M. Fujii, Investigation of polarization effects for high-numerical-aperture first-order Laguerre-Gaussian beams by 2D scanning with a single fluorescent microbead, *Opt. Express* **13**, 10440 (2005).
- [19] Y. Iketaki, T. Watanabe, N. Bokor, and M. Fujii, Investigation of the center intensity of first- and second-order Laguerre-Gaussian beams with linear and circular polarization, *Opt. Lett.* **32**, 2357 (2007).
- [20] P. B. Monteiro, P. A. M. Neto, and H. M. Nussenzeveig, Angular momentum of focused beams: Beyond the paraxial approximation, *Phys. Rev. A* **79**, 033830 (2009).
- [21] T. G. Philbin, Some exact solutions for light beams, *J. Opt.* **20**, 105603 (2018).
- [22] V. V. Kotlyar, S. S. Stafeev, and A. G. Nalimov, Energy backflow in the focus of a light beam with phase or polarization singularity, *Phys. Rev. A* **99**, 033840 (2019).
- [23] K. Volke-Sepulveda, V. Garcés-Chávez, S. Chávez-Cerda, J. Arlt, and K. Dholakia, Orbital angular momentum of a high-order Bessel light beam, *J. Opt. B: Quantum Semiclass. Opt.* **4**, S82 (2002).
- [24] J. E. Curtis and D. G. Grier, Structure of optical vortices, *Phys. Rev. Lett.* **90**, 133901 (2003).
- [25] J. Ng, Z. Lin, and C. T. Chan, Theory of optical trapping by an optical vortex beam, *Phys. Rev. Lett.* **104**, 103601 (2010).
- [26] L.-M. Zhou, K.-W. Xiao, J. Chen, and N. Zhao, Optical levitation of nanodiamonds by doughnut beams in vacuum, *Laser Photonics Rev.* **11**, 1600284 (2017).

- [27] P. Török, P. Varga, Z. Laczik, and G. R. Booker, Electromagnetic diffraction of light focused through a planar interface between materials of mismatched refractive indices: An integral representation, *J. Opt. Soc. Am. A* **12**, 325 (1995).
- [28] A. C. Dogariu and R. Rajagopalan, Optical traps as force transducers: The effects of focusing the trapping beam through a dielectric interface, *Langmuir* **16**, 2770 (2000).
- [29] U. Seifert, From stochastic thermodynamics to thermodynamic inference, *Annu. Rev. Condens. Matter Phys.* **10**, 171 (2019).
- [30] É. Roldán, I. A. Martínez, J. M. Parrondo, and D. Petrov, Universal features in the energetics of symmetry breaking, *Nat. Phys.* **10**, 457 (2014).
- [31] U. Seifert, Stochastic thermodynamics, fluctuation theorems and molecular machines, *Rep. Prog. Phys.* **75**, 126001 (2012).
- [32] S. Ciliberto, Experiments in stochastic thermodynamics: Short history and perspectives, *Phys. Rev. X* **7**, 021051 (2017).
- [33] P. A. Maia Neto and H. M. Nussenzveig, Theory of optical tweezers, *Europhys. Lett.* **50**, 702 (2000).
- [34] A. Mazolli, P. A. Maia Neto, and H. M. Nussenzveig, Theory of trapping forces in optical tweezers, *Proc. R. Soc. Lond. A* **459**, 3021 (2003).
- [35] N. B. Viana, M. S. Rocha, O. N. Mesquita, A. Mazolli, P. A. Maia Neto, and H. M. Nussenzveig, Towards absolute calibration of optical tweezers, *Phys. Rev. E* **75**, 021914 (2007).
- [36] R. S. Dutra, N. B. Viana, P. A. Maia Neto, and H. M. Nussenzveig, Polarization effects in optical tweezers, *J. Opt. A: Pure Appl. Opt.* **9**, S221 (2007).
- [37] B. Richards and E. Wolf, Electromagnetic diffraction in optical systems, II. Structure of the image field in an aplanatic system, *Proc. R. Soc. Lond. A* **253**, 358 (1959).
- [38] C. Rosales-Guzmán and A. Forbes, *How to Shape Light With Spatial Light Modulators* (SPIE Press, Bellingham, 2017).
- [39] M. Born and E. Wolf, *Principles of Optics* (Cambridge University Press, Cambridge, 2019).
- [40] R. S. Dutra, N. B. Viana, P. A. Maia Neto, and H. M. Nussenzveig, Absolute calibration of optical tweezers including aberrations, *Appl. Phys. Lett.* **100**, 131115 (2012).
- [41] R. S. Dutra, N. B. Viana, P. A. Maia Neto, and H. M. Nussenzveig, Absolute calibration of forces in optical tweezers, *Phys. Rev. A* **90**, 013825 (2014).
- [42] K. Diniz, R. S. Dutra, L. B. Pires, N. B. Viana, H. M. Nussenzveig, and P. A. Maia Neto, Negative optical torque on a microsphere in optical tweezers, *Opt. Express* **27**, 5905 (2019).
- [43] R. S. Dutra, P. A. M. Neto, H. M. Nussenzveig, and H. Flyvbjerg, Theory of optical-tweezers forces near a plane interface, *Phys. Rev. A* **94**, 053848 (2016).
- [44] A. R. Edmonds, *Angular Momentum in Quantum Mechanics* (Princeton University Press, Princeton, 1957).
- [45] A. Ashkin, Forces of a single-beam gradient laser trap on a dielectric sphere in the ray optics regime, *Biophys. J.* **61**, 569 (1992).
- [46] C. F. Bohren and D. R. Huffman, *Absorption and Scattering of Light by Small Particles* (Wiley, Hoboken, 1998).
- [47] NIST Digital Library of Mathematical Functions, edited by F. W. J. Olver, A. B. Olde Daalhuis, D. W. Lozier, B. I. Schneider, R. F. Boisvert, C. W. Clark, B. R. Miller, B. V. Saunders, H. S. Cohl, and M. A. McClain (2022), <http://dlmf.nist.gov/10>.
- [48] See Supplemental Material at <http://link.aps.org/supplemental/10.1103/PhysRevResearch.6.023226> for videos of the optically trapped microsphere for different focal heights. From left to right we increase the spherical aberration by moving the sample chamber downwards. The microsphere radius is $a = 1.5 \mu\text{m}$ and the topological charge is $\ell = 8$.
- [49] F. Gómez, R. Dutra, L. B. Pires, G. R. d. S. Araújo, B. Pontes, P. A. Maia Neto, H. M. Nussenzveig, and N. B. Viana, Non-paraxial mie theory of image formation in optical microscopes and characterization of colloidal particles, *Phys. Rev. Appl.* **15**, 064012 (2021).
- [50] Y. Li, L.-M. Zhou, and N. Zhao, Anomalous motion of a particle levitated by Laguerre-Gaussian beams, *Opt. Lett.* **46**, 106 (2021).
- [51] Y. Roichman, A. Waldron, E. Gardel, and D. G. Grier, Optical traps with geometric aberrations, *Appl. Opt.* **45**, 3425 (2006).
- [52] I. A. Martínez, A. Petrosyan, D. Guéry-Odelin, E. Trizac, and S. Ciliberto, Engineered swift equilibration of a Brownian particle, *Nat. Phys.* **12**, 843 (2016).
- [53] D. Raynal, T. de Guillebon, D. Guéry-Odelin, E. Trizac, J.-S. Lauret, and L. Rondin, Shortcuts to equilibrium with a levitated particle in the underdamped regime, *Phys. Rev. Lett.* **131**, 087101 (2023).
- [54] L. B. Pires, R. Goerlich, A. L. da Fonseca, M. Debiossac, P.-A. Hervieux, G. Manfredi, and C. Genet, Optimal time-entropy bounds and speed limits for Brownian thermal shortcuts, *Phys. Rev. Lett.* **131**, 097101 (2023).
- [55] N. B. Viana, M. S. Rocha, O. N. Mesquita, A. Mazolli, and P. A. Maia Neto, Characterization of objective transmittance for optical tweezers, *Appl. Opt.* **45**, 4263 (2006).
- [56] M. I. M. Feitosa and O. N. Mesquita, Wall-drag effect on diffusion of colloidal particles near surfaces: A photon correlation study, *Phys. Rev. A* **44**, 6677 (1991).
- [57] E. Schäffer, S. F. Nørrelykke, and J. Howard, Surface forces and drag coefficients of microspheres near a plane surface measured with optical tweezers, *Langmuir* **23**, 3654 (2007).